

Chapter 5. Technical Systems

5.1 RF

J. Griffin, J. Reid, D. Wildman

5.1.1 Accelerating rf System

Parameters for the PD2 8-GeV synchrotron are listed in Table 5.1.1. The required rf accelerating voltage per turn, $V\sin\phi_s$, and the rf power delivered to the beam per turn, are derived directly from the rate of change of synchronous momentum, $cp(t)$.

Table 5.1.1 Parameters for the PD2 8-GeV Proton Synchrotron

Mean orbit circumference	474.2	m
Cycle repetition rate	15	Hz
Injection kinetic energy	600	MeV
Extraction kinetic energy	8	GeV
Momentum acceptance (95%)	$\pm 1\%$	
Harmonic number	84	
Occupied rf buckets	82	
Rf frequency range	42.0828 to 52.52	MHz
Protons per cycle	2.5×10^{13}	
Average rf power delivered to beam per cycle	444	kW
Injection longitudinal emittance per bunch (95%)	< 0.1	eV-s
Accelerated beam longitudinal emittance per bunch (95%)	< 0.2	eV-s
Transition gamma	13.82	

In Figure 5.1.1(a) the accelerating voltage $V\sin\phi_s$, and the rf power delivered to the beam (as well as $cp(t)$ and the kinetic energy $T(t)$), are shown for a sinusoidal 15 Hz magnet ramp. Figure 5.1.1(b) shows the same parameters for a 15 Hz magnet ramp to which a 12.5% second harmonic component has been added.

Addition of the second harmonic component to the acceleration ramp adds ~5 ms to the acceleration period, while reducing the peak amplitude of the rf power delivered to the beam from 1.42 MW to 1.06 MW. This distributes the power requirement more evenly over the cycle. The second type of the Robinson stability requirements in heavy beam loading conditions is that the power dissipated in the rf source be larger than that delivered to the beam. By distributing the beam power demand over the acceleration cycle, the rf cavity and amplifier dissipation may be equilibrated while still providing an adequate stability margin.

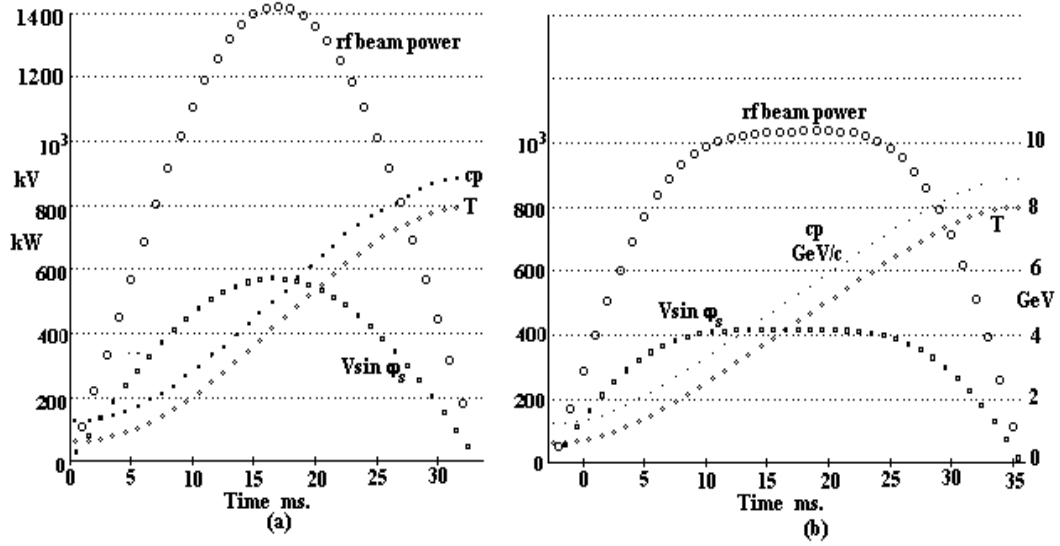


Figure 5.1.1. (a) and (b). Acceleration ramps without and with harmonic component.

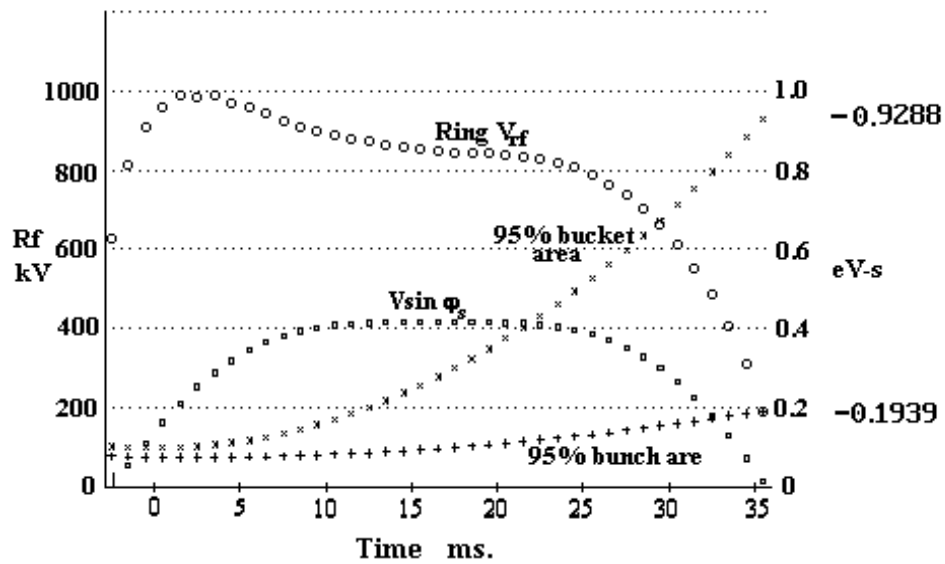


Figure 5.1.2. Rf ring voltage required for generating bucket area from 0.1 to 0.95 eV-s during the acceleration cycle.

In Figure 5.1.2 the ring rf voltage, rf bucket area, and an assumed bunch area consistent with ongoing simulation results are shown. For this calculation the plotted bucket-to-bunch area ratios and attendant bunch lengths are used to calculate the effect of space charge potential well distortion following injection. It is assumed that sufficient

inductance has been introduced into the lattice so that the effective ring Z/n is inductive during acceleration, ranging from $j30\ \Omega$ at injection to $j5\ \Omega$ at extraction. The bunch longitudinal emittance reaches 0.19 eV-s at extraction. The plots are useful for evaluating cavity and amplifier performance at the maximum voltage point and at the maximum power demand point.

The peak rf ring voltage demand, ~ 1 MV per turn, occurs at about 5 ms (46.11 MHz). With twenty cavities, the effective voltage per cavity, V_c is 50 kV. The anode-to-each-gap voltage step-up ratio on the modified cavity is ~ 1.4 at 46 MHz. The effective cavity voltage is $V_c = 2V_g \sin(\Delta)$, where V_g is the voltage at each gap and 2Δ is the gap separation angle (136°). The step-up ratio from tube anode to effective gap voltage V_c is 2.6, so the anode rf voltage becomes 19.23 kV. The measured resonant anode load resistance of the modified cavities at 46 MHz is $5\ \text{k}\Omega$, which transfers to effective cavity shunt impedance $R_{sh} = 33.8\ \text{k}\Omega$. The cavity power dissipation $V_c^2/2R_{sh} = 37\ \text{kW}$. At 46 MHz the accelerating voltage $V_c \sin \phi_s$ is 253 kV (12.65 kV per cavity). With 50 kV gap voltage the phase angle $\phi_s = 14.7^\circ$.

With 82 of 84 buckets occupied with 3×10^{11} (4.88×10^{-8} Coulomb), the average dc beam current is ~ 2.25 A. The very small ϕ_s implies tightly bunched beam with large Fourier component. The Fourier component of rf beam image current i_i , will be ~ 4.5 A, capable of generating 152 kV at the effective cavity accelerating gap if the cavity is tuned to resonance. Through the use of a local phase-lock loop that compares the cathode drive current phase to the anode voltage phase, the cavities are detuned above beam resonance (below transition) so that a real load is presented to the power amplifier tube.

At 46 MHz the beam power requirement is 504 kW (25.4 kW per cavity). The amplifier grid bias, rf drive, and conduction angle may be set such that the anode dissipation is 120 kW. With correct detuning the amplifier will deliver 188 kW to a real load, with efficiency $\sim 61\%$. Effective gap shunt impedance R_o representing the anode dissipation plus cavity losses is defined as $R_o \equiv V_c^2/2P_d$. An effective gap current representing total cavity losses, $i_o \equiv V_c/R_o$. The ratio of beam image current i_i to i_o is defined $Y \equiv i_i/i_o$. In this circumstance the detuning angle $\Theta = \arctan(Y \cos \phi_s) = 34.7^\circ$. The second of Robinson's criteria for beam loading stability is expressed in terms of these factors. The stability factor SF is required to be less than one. In this case $SF = Y \sin(\Theta) \cos(\Theta) / \cos(\phi_s) = 0.347$.

At 23 ms (52.48 MHz), the beam rf power demand peaks at 1.039 MW (52 kW per cavity). At that point the ring voltage demand is 836 kV (41.8 kV per cavity), and $V \sin \phi_s$ is 415 kV (20.8 kV per cavity). The phase angle ϕ_s is 29.8° . Again assuming that the power amplifier operating point is adjusted such that the anode dissipation is 120 kW, the detuning angle Θ becomes 31.9° . The amplifier delivers 198 kW at efficiency 62%. The stability factor $SF = 0.37$.

5.1.2 Large Bore (5-in diameter) Booster Cavity

The longitudinal bucket area and beam power requirements outlined above can be generated with reasonable efficiency and stability by the installation of twenty rf stations of the two-gap design presently installed in the FNAL Booster ring. The beam pipe aperture of the existing accelerating cavities is not adequate for the proposed accelerator. This problem has been addressed and modification of an existing cavity for larger aperture is well under way. [1] Measurements and specifications of the modified cavity are described in Chapter 5 of Ref. [2]. The modified cavities will use recently designed solid-state driver amplifiers. A discussion of the driver amplifier operation, with details of rf drive power, final amplifier screen power, and bias levels necessary to establish desired levels of anode efficiency and dissipation has been prepared by T. Berenc and J. Reid. [3]

The first welded prototype increased aperture cavity has been run at high power with two standard Booster tuners and one Main Injector tuner in the rf test station at MI-60. The high power tests were done without the required ceramic vacuum windows at each end of the cavity. This was a demonstration that the cavity would run with standard Booster frequency and anode voltage waveforms, making a nominal 55 KV peak accelerating volts (see Figure 5.1.3). The maximum voltage that can be achieved with this cavity is expected to be near 65 kV at 52 MHz due to a voltage breakdown limit of the existing ferrite tuner assembly. This limitation may be overcome by increasing the tuner stem connecting inductances, which will cause a slight reduction in the rf voltage at the tuners.

Detailed mechanical drawings for fabrication of a cavity that can be placed in the present Booster tunnel are being prepared. Most of the drift tube assembly has been detailed and dimension checking is presently under way before releasing drawings for fabrication of individual parts. The plan is to have one cavity assembled and ready for testing by late this year (2002). Six ceramic windows (two required per cavity) have been delivered and inspected.

At the relatively high beam current proposed in this upgrade, the most pressing problem in operation of the system will almost certainly be the longitudinal coupled bunch instability due to spurious resonances in the rf system or elsewhere in the ring. Special attention to spurious resonances will be required in the development of the modified aperture cavities. The double gap design of the cavities is particularly sensitive to end-to-end mode excitation, and careful design will be required to damp or eliminate this excitation mode. If these instability considerations can be overcome by a variety of damping techniques, there appears to be no serious barrier to successful installation and operation of these rf systems in the proposed accelerator upgrade scheme.

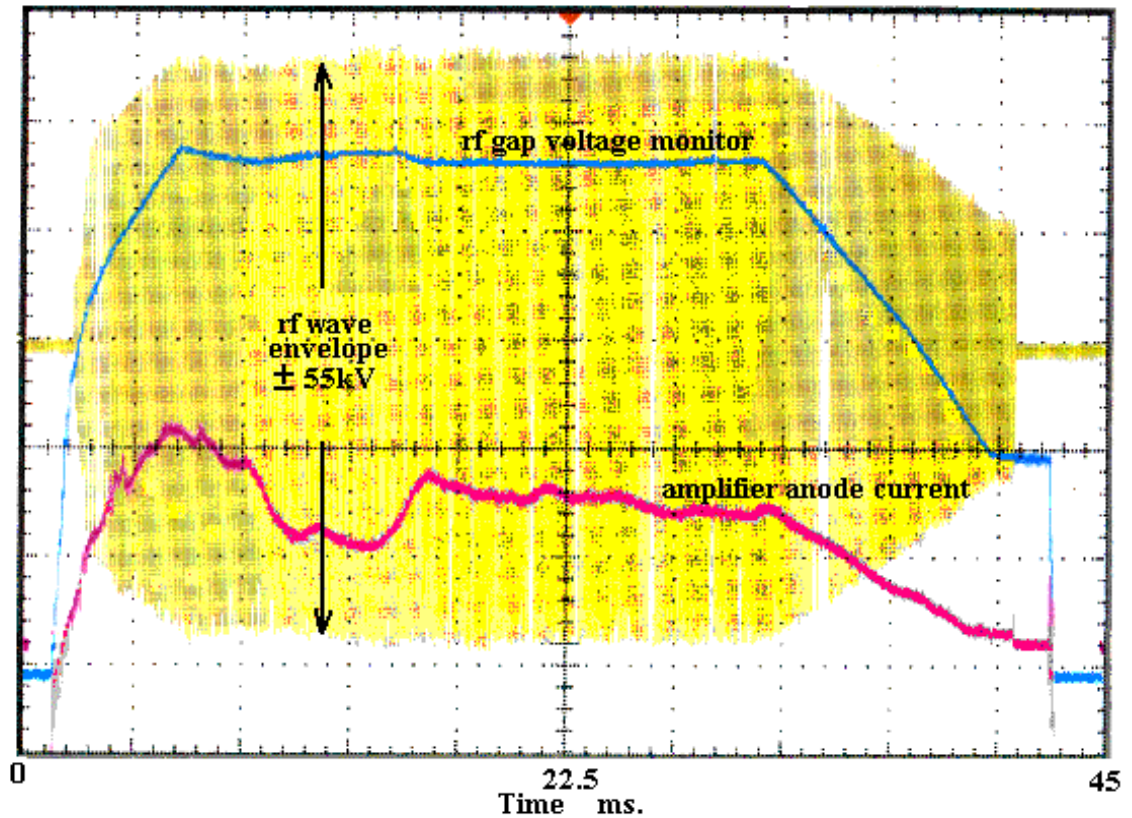


Figure 5.1.3. Large bore prototype cavity running a typical Booster waveform.

5.1.3 Passive Inductance Compensation for Space Charge Potential Well Distortion

In the present operation mode of the Booster approximately 65% of the beam loss on each cycle occurs within the 4-5 ms following injection. (This does not include another ~30% loss that occurs during the injection process.) It is conjectured that this loss results from a combination of transverse and longitudinal space charge effects. [4] It appears likely that this loss mode could increase to an unacceptable level with the proposed beam intensity increase. It has been proposed that longitudinal space charge potential well distortion effects can be eliminated through intentional introduction of inductance into the lattice. [5] Simulation studies of an earlier version of a high intensity proton driver (cf. Ref. [2], Ch.5-8, 9) have indicated that a dramatic reduction of losses during injection and acceleration are possible with insertion of appropriate values of inductance. The proposition has been tested experimentally in the LANL 800 MeV Proton Storage ring (PSR), and in the KEK 12 GeV proton synchrotron. [6,7] In each case dynamical predictions regarding effective rf focusing force were found to be correct.

The PSR operates at harmonic number one and rotation period ~358 ns, with gated injection bunches ~300 ns. The introduced inductance consisted of two tanks of $M_4C_{21}A$ Toshiba ferrite, each containing 30 cores and presenting inductance ~4 μH . This was

originally thought to be about two-thirds of the inductance necessary to compensate exactly for the space charge induced longitudinal field seen by particles in the bunch. The goal of the exercise was to reduce particle leakage from the rf buckets into the space between bunches, where free protons may interact with trapped electrons causing e-p instability. The focusing force enhancement by the inductance is the result of interaction of the line charge derivative of the beam bunch with the inductance. The inductive reactance must be effective over a frequency range defined by the Fourier components of the charge distribution. Because of the relatively low rotation frequency and long bunches the frequency response of the introduced ferrite was well matched to the requirement.

The initial results of the exercise were sufficiently encouraging so that continued routine operation of the PSR with the installed inductances was initiated. However, at substantially increased intensity it was found that the inserts introduced a severe self-bunching instability near 72 MHz, preventing continued operation in this mode. Careful study of an equivalent ferrite geometry reveals a TM_{01} radial transmission line resonance near 84 MHz with $Q \sim 4-5$.

It has been further established that heating the ferrite to $\sim 130^\circ \text{C}$ increases the imaginary part of the permeability $j\mu''$ and reduces the Q of the resonance to a level near 1.5 - 2, at which level the PSR can be operated successfully. An added and serendipitous effect is that the required heating also increases the real part of the permeability μ' such that the introduced inductance equals or exceeds that necessary for exact compensation. The result is that the roughly rectangular injected charge distribution creates, in addition to the rf system field, self generated longitudinal barriers at each end of the injected distribution such that the length and amount of injected beam can be increased to near the rotation period. The net result is that the PSR is now capable of operation at a level near 9.6 μC per cycle, $\sim 40\%$ larger than the goal of the most recent rf system upgrade. [8]

In an initial attempt to address the cause of beam losses observed during the Fermilab Booster cycle, two inductive inserts similar to those in the PSR have been installed in the Booster. It is known, of course that, because the Booster accelerates from 400 MeV to 8 GeV using a harmonic number of 84, the frequency response of the introduced ferrite will not be well matched to the Fourier components of the beam.

Nevertheless, as a first step in evaluating their usefulness, it has been decided to install two inserts similar to those installed in the PSR. This is expected to compensate $\sim 20\%$ of the estimated space charge forces near injection. One real concern is the possibility that the inserts may excite a coupled-bunch instability driven by the known TM_{01} resonance at 73 MHz. At beam intensities up to 4.6×10^{12} no evidence has been observed of unusual signals near 73 MHz on the Booster resistive wall monitor. Unfortunately, no discernable improvement has been seen in the initial beam losses since the introduction of the inductive inserts in the Booster. One possible explanation is that the inductance of the two inserts is too low (about 10 μH) to show any effect. Six to eight more inserts will be added in the next step.

The PD2 is an ideal candidate for inductive inserts since the proton intensity will be five times greater than the present Booster. An R&D effort should be started to identify alternative higher frequency ferrites that would be a better match for the shorter PD2 bunches.

References

- [1] J. Griffin, "Proposal to Rebuild Damaged Booster RF Cavity with Significant Improvement in Aperture, Gap Voltage, and Power Delivery Capability)," (1999).
- [2] "The Proton Driver Design Study," FERMILAB-TM-2136 (Dec. 2000).
- [3] T. Berenc and J. Reid, "A Solid-State Driven Power Amplifier Design for the Booster RF Cavities)," RFI Technote 023, (8-2001).
- [4] M. Popovic and C. Ankenbrandt, "Space Charges in the Fermilab Booster," Space Charge Tune-Shift Workshop, AIP Proc. 448, 128, (1998).
- [5] A. Sessler and V. Vaccaro, "Passive Compensation of Longitudinal Space-Charge Effects in Circular Accelerators - The Helical Insert," CERN 68-1, ISR Div. (1968).
- [6] K. Koba et. al. "Longitudinal Tuner Using High Permeability Material," R.S.I. 70-7 (1999).
- [7] J. Griffin, K.Y. Ng, Z.B. Qian and D. Wildman, "Experimental Study of Passive Compensation of Space Charge Potential Well Distortion at the Los Alamos National Laboratory Proton Storage Ring," Fermilab FN-661, (1977).
- [8] R.J. Macek et. al, "Electron Proton Two-Stream Instability at the PSR," 2001 PAC Proceedings, Chicago, p.688, 2001.

5.2. Magnets

V. Kashikhin, A. Makarov and J. -F. Ostiguy

In the first design study (referred to as Study I) published in December 2000 [1], the Proton Driver was envisioned to be a machine capable of delivering 1 MW of beam power at 16 GeV. The design parameters assumed in this new study are more modest: 380 kW at 8 GeV. From a magnet standpoint, the principal change is a reduction in the good field aperture requirement from $12.7\text{ cm} \times 22.86\text{ cm}$ (5 in \times 9 in) to $10.16\text{ cm} \times 15.25\text{ cm}$ (4 in \times 6 in). This reduction leads to smaller magnets, lower overall stored magnetic energy and reduced operating costs. In Study I, we chose a special water-cooled stranded cable to suppress eddy currents in the conductors. While this remains an interesting solution, stranded cable is expensive. Furthermore, the technology for making electrically and mechanically reliable joints with this type of conductor is not well-established. For this iteration, we revisited our choice and concluded that conventional water-cooled conductor coils can be used. Both fabrication technology and costs are well-understood; the compromise is reduced operation efficiency.

One of the principal considerations in designing a high intensity proton synchrotron is to limit space charge induced tune shift and tune spread in order to ensure dynamic stability. This is accomplished in two ways: by keeping the machine circumference small and by spreading out the proton distribution transversely. The former strategy implies rapid cycling; the latter implies large aperture.

Aperture is a principal cost driver since magnet overall size, fabrication costs and power consumption and power supply costs are directly proportional to stored magnetic energy. Aperture is determined not only by space charge considerations, but also by the type of vacuum pipe employed. Additional aperture margin may also be needed to keep losses at a level compatible with safety requirements. Because of very substantial eddy current induced losses, a conducting beam pipe cannot be used. One possible solution is a ceramic beam tube with very thin conducting strips disposed on the inner surfaces to minimize beam impedance. This approach is costly in terms of physical aperture because ceramic walls have to be considerably thicker than metallic walls for mechanical reasons. The Proton Driver magnets use a strategy employed for the Fermilab Booster magnets : the entire magnet is put inside an evacuated enclosure. One drawback is that special care is needed in order to achieve satisfactory vacuum. This is important since beam loss induced activation is an important issue for a high intensity machine.

The Proton Driver is based on a separated function lattice with dipoles and quadrupoles on a common bus. The presence of a large energy dependent space charge tune shift and tune spread dictates the need for tight tune control during the entire acceleration cycle. For this reason, dipole/quadrupole tracking errors are a special concern. A tracking error is

equivalent to momentum offset error and results in a tune shift of magnitude

$$\Delta\nu = \xi_{\text{uncorrected}} \left[\frac{\Delta G}{G} - \frac{\Delta B}{B} \right] = \xi_{\text{uncorrected}} \left[\frac{\Delta(G/B)}{(G/B)} \right] \quad (5.2.1)$$

where $\frac{\Delta G}{G}$ and $\frac{\Delta B}{B}$ are respectively the relative gradient and main dipole field errors. Note that the tune variation is proportional to $\xi_{\text{uncorrected}}$, the *uncorrected* chromaticity because, in the context of a quadrupole tracking error, there is no closed orbit error and the chromaticity correction sextupoles have no effect.

The magnitude of the tolerable tune shift is debatable. In the context of this study, we *conservatively* demand

$$\Delta\nu < 0.01 \quad (5.2.2)$$

during the *entire* cycle. This requirement is based on the ISIS experience, where the ability to control the tune at that level proved to be necessary to avoid specific resonances at extraction. It is conceivable that criterion (5.2.2) can be relaxed. Problematic resonances could be avoided; furthermore, space charge forces scales as $1/\gamma$ and tracking should be less critical an issue as time progresses during the acceleration cycle. Detailed simulations which are beyond the scope of this study would be necessary to validate relaxed tune control requirements.

Some rapid cyclic machines, like the Fermilab Booster, use combined function magnets to economize space. Good tracking is naturally obtained by operating far away from saturation (below 1 T). As already mentioned, the Proton Driver employs separate function magnets with bending dipoles operating at an aggressive 1.5 T peak field. The field strength is determined by two requirements. First, the circumference ratio between the Main Injector and the Proton Driver should be a simple rational fraction to allow synchronous beam transfers. Second, the total circumference should be as small as possible in order to minimize the space charge tune shift. While magnet transfer functions start deviating from linearity above 1 T, quadrupole and dipole magnets can be designed with matched saturation behaviors. The residual tracking error (on the order of a percent or two) is handled by an independently powered active quadrupole correction system. This system also has the ability to compensate for the tune shift dependence on energy during acceleration. Note that above 1.5 T, good dipole/quadrupole matching rapidly becomes more difficult.

5.2.1. Dipoles

The Proton Driver dipole is a conventional H-magnet design. Field homogeneity is preserved at high excitation by profiled pole edges and by the presence of circular holes in the center of the poles. The lamination cross-section is shown in Figure 5.2.1; a list of relevant parameters is presented in Table 5.2.1. The dipoles are excited so as to produce a magnetic field strength of the form

$$B(t) = B_0 - B_1 \cos(\omega t + \phi) + 0.125 B_1 \sin(2\omega t + 2\phi) \quad (5.2.3)$$

Table 5.2.1. Proton Driver II Main Dipole Magnet Parameters

Peak Dipole Field	1.5	Tesla
Good Field Aperture	101.6×152.4	mm ²
Physical Aperture	101.6×273.1	mm ²
Field Homogeneity	± 0.0005	
Magnet Length	5.72	m
Cycle Frequency	15	Hz
Peak Current	5170	A
Conductor Dimensions	20.2×15	mm ²
Conductor cooling hole diameter	10	mm
No of turns/pole (3 conductors & top/bottom coils in parallel)	12	
Lamination Thickness	0.35	mm
Lamination Material	Si-Fe M17	
Inductance	18	mH
DC Resistance	4.7	mOhm
Stored Energy	0.063	MJ
Coil Losses	115	kW
Core Losses	16.3	kW
Core mass	37,000	kg
Peak Terminal Voltage	4.85	kV
Water Pressure Drop	10	bar
Water Flow	1.7	l/s
Water Temperature Rise	17	deg C

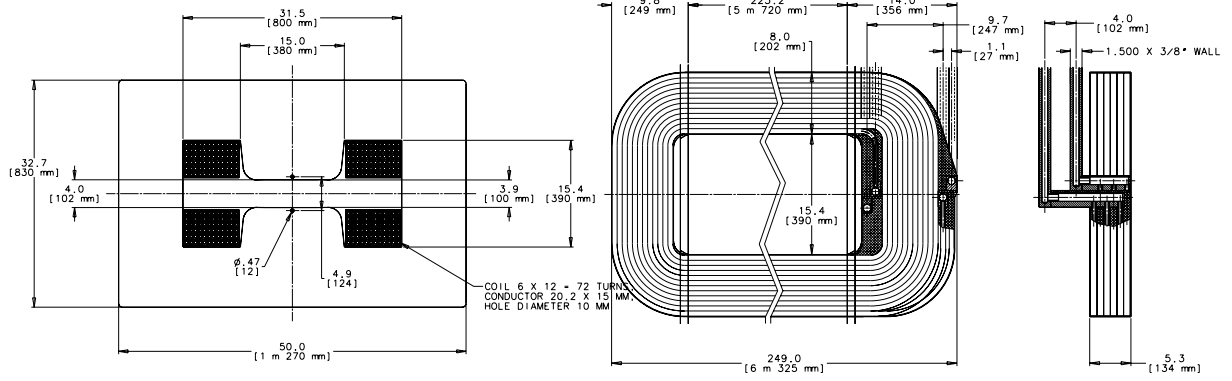


Figure 5.2.1. Proton Driver dipole cross-section and coil detail. Note the circular holes in the center of the poles. Note also the parallel connections at one of the coils extremities.

where B_0 is the injection field, B_1 is the magnitude of the fundamental component, $\omega/2\pi = f = 15$ Hz and ϕ is a constant phase factor. The second harmonic component is introduced to reduce the maximum value of dB/dt . Since the instantaneous RF accelerating voltage is proportional to dB/dt , the peak voltage required from the RF system cost is reduced, resulting in a substantial reduction in RF system costs. The magnetic field ramp and its derivative are shown in Figure 5.2.2.

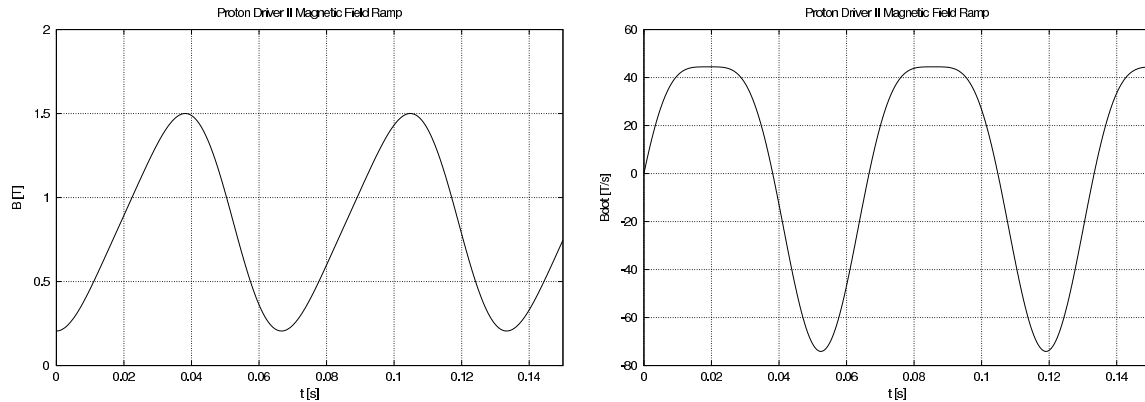


Figure 5.2.2. Magnetic field ramp and its derivative for 8 GeV operation ($B_0 = 0.853$ T, $B_1 = 0.629$ T). The RF accelerating voltage is proportional to the derivative of the magnetic field. The maximum of the derivative occurs on the down ramp. This value determines the maximum magnet terminal voltage although no beam is accelerated at that time.

In an iron dominated dipole, good field homogeneity can be achieved over the entire extent of the physical vertical aperture, that is, all the way to the pole surfaces. However, field homogeneity over the horizontal extent of the aperture requires a certain amount of pole overhang. For a given field homogeneity, the required horizontal extent of the physical aperture is minimized by shimming the pole pieces edges. A wide variety of shim geometries are possible. The optimality of a design can be accessed by comparing the achieved physical horizontal extent to a theoretical estimate developed by Klaus Halbach [2]. Re-

ferring to Figure 5.2.3, assume the origin of the x -axis is situated exactly at the pole edge and that the pole continues to infinity for $x > 0$. At any fixed horizontal position x and, in particular at $x = 0$, the complex field is an even function of the vertical position y can be expanded in a Fourier series of the form

$$H_y + jH_x = \sum_{n=-\infty}^{\infty} C_n \exp \frac{n\pi z}{g} \quad (5.2.4)$$

where g is the total vertical gap, the C_n are complex constant coefficients and $z = x + jy$. Since the field is finite, the coefficients C_n vanish for $n > 0$ and $C_0 = H_{y0}$ represents the field deep into the aperture region. Let d be the pole overhang, as defined in Figure 5.2.3. Without shims, the first few low order harmonics dominate the field deviation from uniformity. Considering only the first ($n = -1$) harmonic, the field error at the edge of the good field region is

$$\frac{\Delta B}{B} = \frac{\Delta H_y}{H_{y0}} \simeq \frac{1}{H_{y0}} \Re\{C_1\} = h_1 \exp \frac{-\pi d}{g} \quad (5.2.5)$$

With no shim, the first spatial harmonic dominates. A properly designed shim should suppress the first harmonic and the second harmonic dominates. Using these results, Halbach found that a simple two-parameter empirical relation of the form

$$\frac{\Delta B}{B} \simeq \lambda_1 \exp \frac{-\lambda_2 d}{g} \quad (5.2.6)$$

is generally an adequate predictor of field homogeneity. The values of λ_1 and λ_2 depend weakly on the pole geometry and are obtained by fitting results obtained numerically from two-dimensional calculations. Figure 5.2.1. shows the predicted amount of overhang necessary to achieve a field homogeneity $\frac{\Delta B}{B}$ for both shimmed and unshimmed magnets. For a given homogeneity, the amount of required overhang increases proportionally to the magnet gap. Thus, any increase in vertical aperture of the magnet – e.g. to accommodate a thick ceramic vacuum pipe – would result in a proportional increase in overall horizontal size. Figure 5.2.5 presents calculated field homogeneities achieved by the Proton Driver II dipole magnet. For this magnet, the ratio $d/w \simeq 0.6$ and we note that the achieved homogeneity is consistent with the prediction from Halbach's formula.

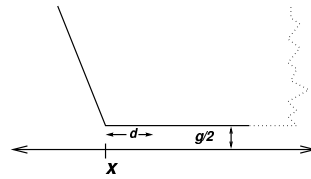


Figure 5.2.3. Idealized semi-infinite dipole magnet with pole overhang d and full gap g . The horizontal origin is exactly at the outer edge of the pole.

In a rapid cycling magnet, the presence of eddy currents is a source of potential technical difficulties. Eddy currents are induced both in the magnetic core and in the conductors. Eddy currents in the core are largely suppressed by the laminated core construction which

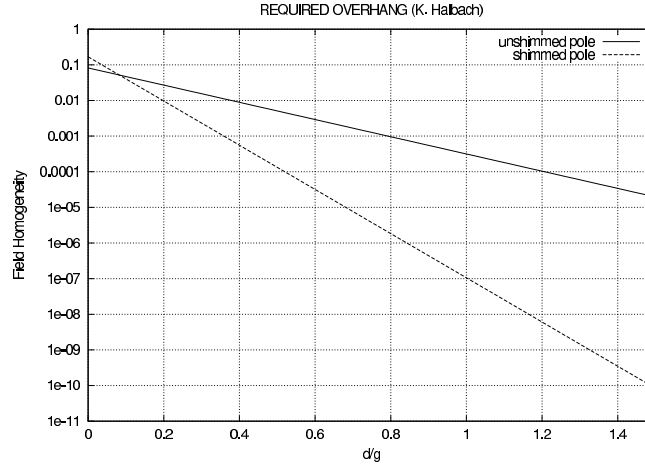


Figure 5.2.4. Amount of overhang required to achieve a given homogeneity as predicted by Halbach's formula.

impedes their flow in the longitudinal direction. As long as the lamination thickness is smaller than the skin depth, the principal effect of eddy currents in the core is to increase losses.

The Proton Driver magnet cores are assembled from 0.014 in (0.35 mm) thick isotropic Si-Fe laminations (M17 or M19). This material has a substantially higher resistivity than the low carbon steel used in low repetition rate synchrotron magnets. It offers a reduced coercivity which helps minimize remanent fields at injection. The main drawbacks are reduced high field permeability and saturation magnetization. At 15 Hz, the skin depth in electrical steel is $\delta \simeq 1 \text{ mm} = 0.040$. One might question why even thinner laminations are not used. The answer is that very thin laminations are hard to handle and complicate the magnet assembly process. Furthermore, since laminations are coated with an insulator, thin laminations result in magnets with a less favorable stacking factor.

Core losses are difficult to compute and are usually estimated from experimental data. Virtually all data commonly supplied by manufacturers corresponds to measurements performed with a sinusoidal excitation at 50 or 60 Hz. Not only does the Proton Driver operate at 15 Hz, but the excitation also has a non-zero average component I_0 , which renders the hysteresis loops asymmetric. As a reference, careful measurements were performed on a small core made out of M17 laminations. The results are summarized in Figure 5.2.7. For 0.014 in thick laminations with a DC bias equal to 50% of the maximum (1.5 T) field amplitude, the measured losses are on the order of 0.2 W/lb (0.44 W/kg).

Eddy currents induced in conductors are potentially problematic. Assuming that the total current circulating through each conductor is externally constrained, the sum of the induced currents over the conductor cross-section must add up to zero. However, the current distribution is not uniform, resulting in higher losses, or equivalently in a higher effective resistance. As long as the non-uniformity of the current distribution does not affect the

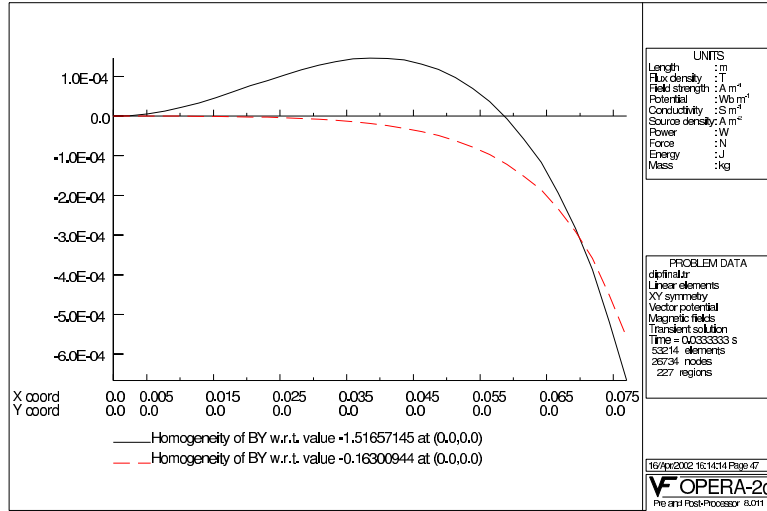


Figure 5.2.5. Proton Driver dipole field homogeneity at minimum and maximum excitations.

field homogeneity, the main issues are providing adequate cooling and minimizing operating costs.

For a rectangular conductor immersed in a uniform time-varying magnetic field $B_0 \sin(\omega t)$, it can be shown that the power losses are given by

$$P = \omega^2 B_0^2 A a^2 / 16\rho \quad (5.2.7)$$

where A is the conductor area, a is the conductor width and ρ is the resistivity. Eddy currents can be reduced either by reducing the conductor cross-section or by reducing the magnetic field in which it is immersed. Reducing the conductor area increases the number of turns N and therefore the magnet terminal voltage, since the inductance scales like N^2 . To keep the voltage at a reasonable level it becomes necessary to connect multiple turns in parallel. The Proton Driver magnet coils use groups of three conductors connected in parallel. In addition, the coils from the top and bottom coils are also connected in parallel. The electrical and mechanical connections in the end regions are shown in detail in Figure 5.2.1. Note that the conductors are not transposed. Although transposition would reduce losses slightly, it would also render connections in the end region very complex and cumbersome.

In Study I, eddy current power loss problems were completely side-stepped by the use of a special water cooled stranded conductor. Because of the small strand cross-section, eddy currents were reduced to the level of a minor perturbation and could essentially be ignored. Aside from the technology required to produce reliable electrical and mechanical joints, the main drawback of the stranded conductor is its high cost, about an order of magnitude more expensive than conventional copper conductor. For this study, the possibility of using conventional solid water cooled conductors has been revisited. Figure 5.2.7 presents the result of an eddy current computation.

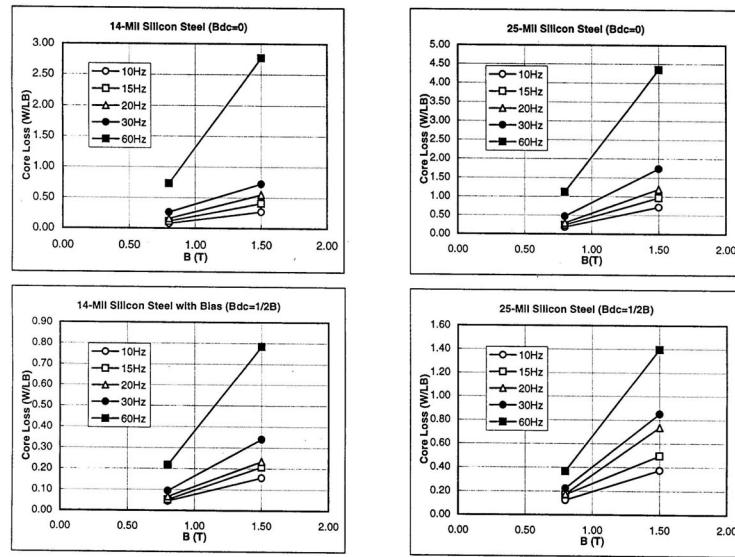


Figure 5.2.6. M17 Electrical steel loss measurements for 14 mil (0.35 mm) and 25 mil (0.64 mm) laminations. The measurements were performed from 10 to 60 Hz, with and without a 50% DC bias in the excitation.

Eddy current losses reach a substantial level in the conductors closest to the edge of the pole, in the fringe field region. To take advantage of the fact that the magnetic field is predominantly vertical in that region, a rectangular (as opposed to square) conductor is employed. Relatively high losses affect approximately 20% of the total coil cross section; however, localized heating should be prevented by good thermal contact between conductors. The relatively uniform coil temperature will be determined by the total average power dissipation over the entire coil area. As already mentioned, conventional water-cooled solid copper coil is a well-understood technology. Compared with stranded conductors, the trade-off is reduced operational efficiency vs reduced up-front fabrication costs.

It is worth mentioning that in principle, the lossier conductors could be moved away from the highest field region. This can be accomplished by increasing the width of the area available for the coil or by constructing a specially shaped coil. Because of time constraints, this possibility was not explored. The solution adopted results in the simplest, easiest to fabricate coils.

5.2.2. Quadrupoles

The Proton Driver quadrupoles are four-fold symmetric magnets. The cross-section is shown in Figure 5.2.8. Both horizontal and vertical focusing quadrupoles are identical and the aperture radius is set to accommodate a rectangular good field region of the same size as the dipoles'. A common current bus is used to make the quadrupole gradient and

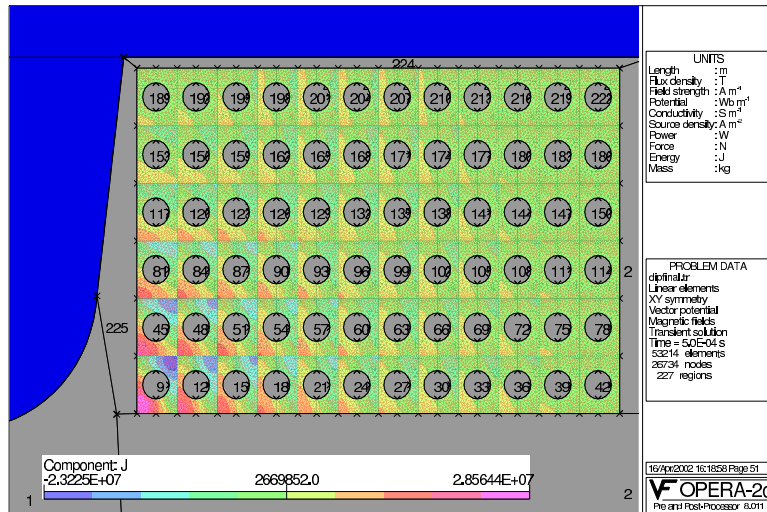


Figure 5.2.7. Eddy current distribution in the conductors. Note that the distribution is most uneven in conductors located near the pole edge.

dipole strength track dynamically. The number of turns and length of the quadrupole are selected so as to match optical and physical requirements at low field. In addition, at high field, the gradient/dipole strength ratio must remain as constant as possible. This requirement effectively limits the maximum achievable gradient. For the required aperture, when the quadrupole pole tip field reaches 0.84 T, the field at the edges of the truncated hyperbolic profile reaches approximately 1.5 T, and saturation begins to affect the linearity of the relation between quadrupole strength and excitation. Note that saturation in backleg region also affect nonlinearity; however, this effect can in principle be controlled by adjusting the backleg width. Note that for a four-fold symmetric quadrupole saturation does not adversely impact field quality since all harmonics except those of order $4n$ ($8n$ -pole) are suppressed: the first allowed harmonic is the 12-pole. Figure 5.2.9 is a plot of the tracking error as a function of the excitation current. At 8 GeV, the deviation is on the order of 2.0%.

5.2.3. Other Magnets

The Proton Driver II sextupole magnets are six-fold symmetric with an aperture radius sufficient accommodate a rectangular region of dimensions $10.16 \times 15.25 \text{ cm}^2$. They are grouped in families powered with independent programmable power supplies. No particular difficulties are anticipated.

Operational experience with machines such as ISIS demonstrates that in addition to good tune control, good orbit control during the entire acceleration cycle is one of the keys to loss minimization. This is not entirely surprising since small orbit changes typically result in small tune perturbations caused by change in overall orbit length and quadrupole

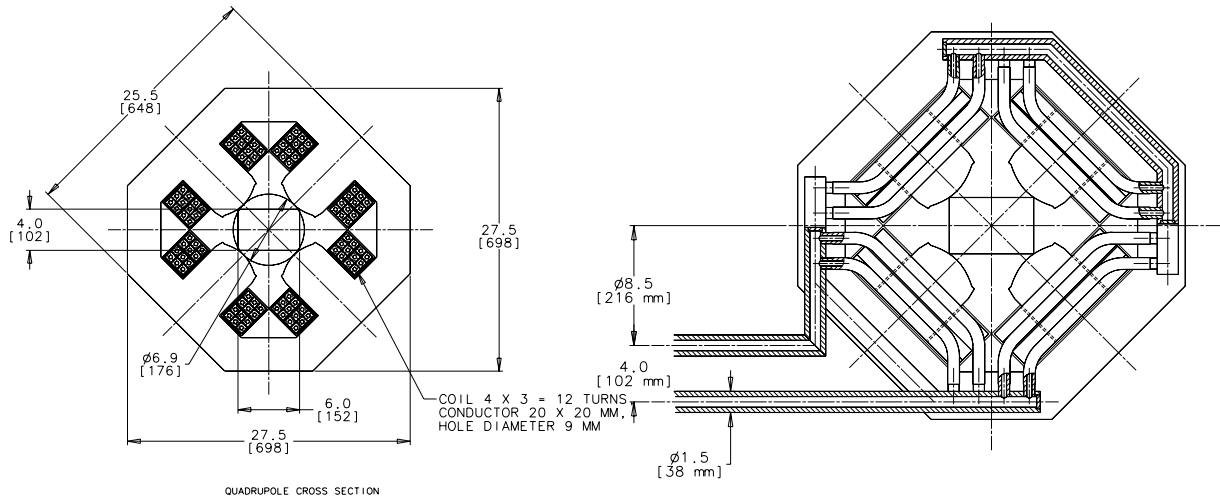


Figure 5.2.8. Proton Driver II quadrupole cross-section and coil detail.

Table 5.2.2. Proton Driver II Quadrupole Magnet Parameters.

Peak Gradient (8 GeV)	9.5626	Tesla/m
Pole Tip Field (8 GeV)	0.84	Tesla
Gradient Homogeneity	± 0.001	
Aperture (Inscribed circle radius)	8.8	cm
Peak Current	5170	A
Steel Length (F & D)	1.2	m
No of Turns/pole	6 (2 cond in parallel)	
Inductance	1.3-1.5	mH
Conductor Dimensions	20×20	mm ²
Conductor cooling hole diameter	9	mm
Coil Losses	31	kW
Max Terminal Voltage	0.4	kV
Lamination Area	0.24	m ²
Lamination Thickness	0.35	mm
Lamination Material	Si-Fe M17	
Core mass	2200	kg
Core losses	1	kW
Water Pressure Drop	10	bar
Water Flow	0.32	l/s
Water Temperature Rise	23	deg C

feed-down in sextupoles. The Proton Driver has a full complement of correctors and no particular difficulties are anticipated in building satisfactory magnets.

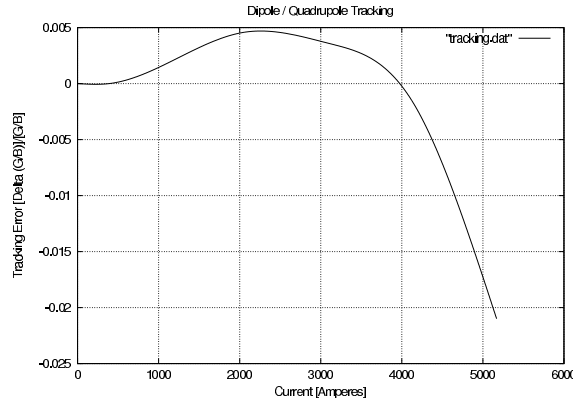


Figure 5.2.9. Normalized Quadrupole/Dipole strength tracking. At 8 GeV (common bus current of 5170 A), the deviation is approximately 2 %. This error is compensated by an independent active correction system.

5.2.4. AC Magnetic Measurements

Henry Glass

The goal of magnetic measurements for the proton driver dipole is to verify field homogeneity at 15 Hz operation. The usual tool for measuring field quality is the rotating harmonics coil. This is usually operated in DC mode; however there is some experience at Fermilab in using such coils to collect AC data. The most direct experience is in measurements of Booster gradient magnets being done in April-May of 2002. In this case a coil of length 1.0 m is installed within the magnet aperture to sample the field quality at various locations, e.g., within the body or at the magnet ends. Custom fixtures are built to support the probe at these locations. The coil has a tangential winding to measure the multipole components, and two pairs of bucking coils to subtract out dipole and quadrupole components. For the proton driver magnet, the situation is simplified by the use of separated function dipoles rather than gradient magnets. In dipoles, there is a greater tolerance of small probe positioning errors. Also, one only needs a pair of dipole bucking windings in addition to the tangential winding. Because of magnet sagitta, it is preferred to use a short coil with length in the range 0.5 - 1.0 m, rather than attempt to build a coil as long as the magnet. In this case, one sacrifices the ability to use the coil to measure total integrated field strength. However, one can measure the total strength using either a stretched wire system or, preferably, a coil wound on a rigid curved form matching the magnet axis curvature. The rotating coil diameter should be chosen as large as possible to have maximum sensitivity to high order harmonics. The constraint is the vertical aperture of 101.6 mm; the probe should be undersized by a few mm to allow for free rotation and probe support fixturing. Since the horizontal aperture is larger (152.4 mm), it is necessary to position the probe not only at the aperture center, but also displaced horizontally at about plus and minus 50 mm from the center to map the entire good field region.



Figure 5.2.10. AC Magnetic Measurement Setup used for a Booster Combined Function Magnet.

5.2.5. Research and Development

High voltage operation is a serious concern. The dipole magnets have a maximum terminal voltage on the order of 5 kV; in the proposed resonant configuration, the maximum voltage to ground reaches approximately 3.3 kV. Electrical insulation is an important issue for magnet long term reliability. Fermilab currently has limited experience with high voltage magnet fabrication and operation. Insulation weaknesses generally need to be spotted experimentally and corrected by trial and error; this can be both tricky and time-consuming. The ISIS synchrotron in operation at Rutherford Lab in the UK has been operating reliably at a significantly higher voltages ($\simeq 10$ kV) than those envisioned for the Proton Driver. Active collaboration and exchanges with RAL would likely be beneficial.

Another source of concern is the fact that the entire magnet is to be placed inside an evacuated enclosure. Special precautions will be needed during the assembly process to avoid degassing that would lead to poor vacuum.

The presence of metallic strips to reduce the beam impedance will perturb the field. While the perturbation can probably be predicted reliably through calculation, it should be carefully measured.

The new Proton Driver lattice uses two types of dipoles. The shortest one is approximately 1 m (1.06 m) long and would make a good candidate for an R&D prototype. Building such a magnet would lead to better understanding of coil fabrication high voltage insulation, and vacuum issues. Furthermore, power loss estimates and cooling effectiveness could be confirmed.

Although we opted not to use stranded water-cooled conductors in the context of this second study, this type of conductor remains an interesting option for rapid cycling synchrotrons. An R&D program should address the problem of making reliable electrical and mechanical joints and other aspects of coil fabrication using water-cooled stranded cable.

Finally, an interesting avenue for future R&D would be an investigation of super-ferric magnet technology. In recent years, a new generation of Nb-Ti superconducting cable has been developed for applications in power generation and transmission. The cable has insulated filaments with a diameter as small as $0.1\text{ }\mu\text{m}$ embedded in a Cu-Ni alloy matrix. Superconducting coils would result in substantial savings in overall magnet size and power consumption; these savings may be substantial enough to offset the additional costs and complexity engendered by the cryogenic system.

5.2.6. References

- [1] The Proton Driver Design Study, Fermilab TM-2136, December 2000.
- [2] A.W. Chao and M. Tigner Eds., *Handbook of Accelerator Physics and Engineering*, World Scientific, 1999.

5.3 Power Supplies

C. Jach, D. Wolff

In this section are described the power supplies required for the PD2 8-GeV synchrotron. A resonant network powers the main dipoles and quadrupoles of the synchrotron. The design is similar to that in Chapter 7, Ref. [1], namely, a dual-harmonic resonant system. It is a 15-Hz resonant circuit with a 12.5% second-harmonic (30-Hz) component. A detailed description of the system can be found in Ref. [1]. The dual-harmonic magnet current and voltage waveforms are shown in Figure 5.3.1.

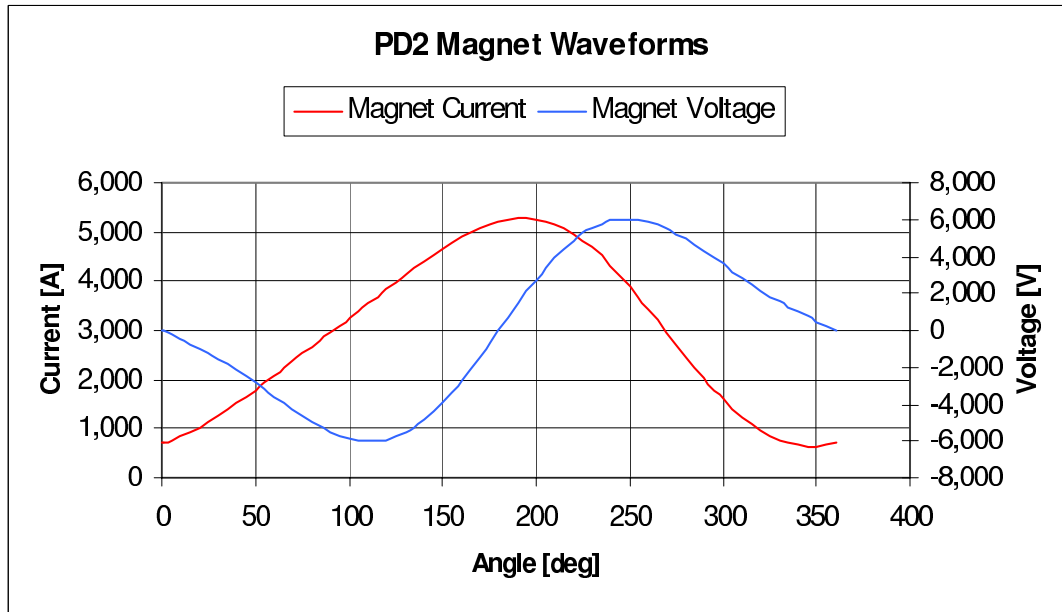


Figure 5.3.1. Magnet current and voltage waveforms.

This network consists of:

- 10 resonant circuit cells with 1 long dipole, 1 short dipole, and a set of quads (D and F) with total inductance of 25.1 mH.
- 10 resonant circuit cells with 1 long dipole, and 2 sets of quads with total inductance of 27.9 mH.
- 2 resonant circuit cells with 7 sets of quads with total inductance of 19.6 mH

Each resonant circuit cell consists of an equivalent magnet (L_m), a main choke (L_{ch}), a main capacitor bank (C), an auxiliary choke (L_1), and an auxiliary capacitor bank (C_1). All resonant circuit cells are connected in series. Power supplies are inserted into the resonant network at or near virtual ground points. Figure 5.3.2 shows a typical resonant circuit cell. Table 5.3.1 lists the inductance and dc resistance of the magnets. Table 5.3.2

are the parameters of the power supply system. Figure 5.3.3 shows the dual-resonant frequencies at 15 and 30 Hz of this system.

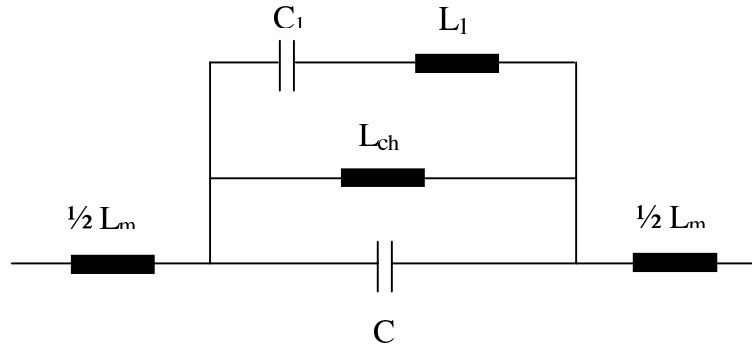


Figure 5.3.2. Typical resonant cell diagram.

Table 5.3.1. Magnet Load Parameters

Parameter	Unit	Value
Dipole, B1		
Length	m	5.646
Inductance	mH	18.9
DC resistance	m Ω	4.7
Total number		20
Dipole, B2		
Length	m	1.188
Inductance	mH	3.4
DC resistance	m Ω	0.9
Total number		10
Quadrupole, QF		
Length	m	1.261
Inductance	mH	1.5
DC resistance	m Ω	2.2
Total number		44
Quadrupole, QD		
Length	m	1.126
Inductance	mH	1.3
DC resistance	m Ω	2.2
Total number		44

Table 5.3.2. Main Magnet Power Supply Parameters

Parameter	Unit	Value
Magnet current:		
- peak	A	5,200
- dc	A	3,000
- ac, 15 Hz	A	2,200
- ac, 30 Hz	A	280
Total magnet inductance	H	0.535
Total magnet DC resistance	Ω	0.297
Magnet peak voltage to ground	V	3,050
Magnet peak stored energy	kJ	7,200
Number of resonant cells		22
Resonant cell main choke peak stored energy	kJ	318
Resonant cell aux. choke peak stored energy	kJ	72
Resonant cell main capacitor bank peak stored energy	kJ	133
Resonant cell aux. capacitor bank peak stored energy	J	107
Power supply voltage, peak	V	$\pm 2,000$
Power supply current, peak	A	5,200
Number of power supplies		4

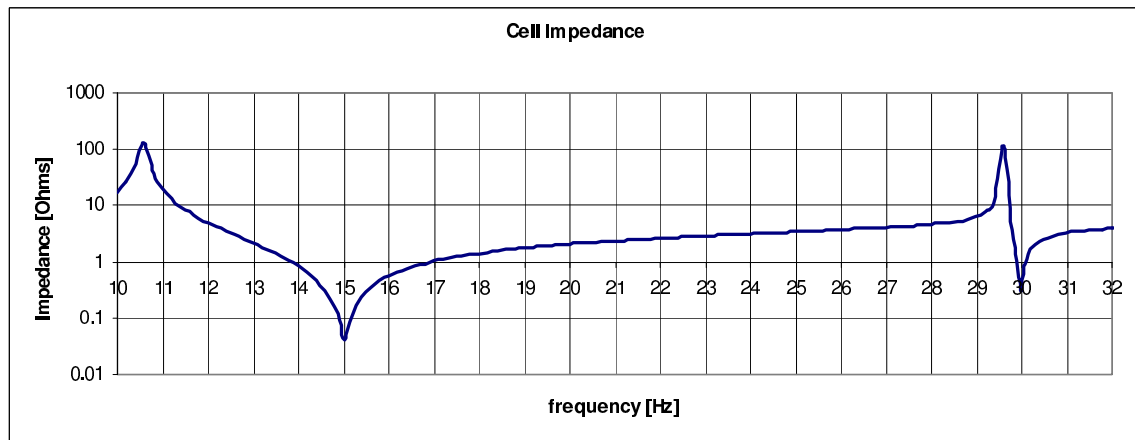


Figure 5.3.3. Single cell frequency response.

References

- [1] "The Proton Driver Design Study," FERMILAB-TM-2136 (December 2000).

5.4. Vacuum

T. Anderson

5.4.1 Design Overview

The PD2 ring vacuum system is a 474-m continuous vacuum chamber composed of magnets, short sections of tubing, bellows, ion pumps, valves, and instrumentation. From a vacuum design standpoint there is little difference between the PD1 ring vacuum system and that of PD2. Both systems use the "canned magnet" design for the magnets and therefore system performance will be limited by the out-gassing rates we are able to achieve in the magnet laminations and coils. Table 5.4.1 below shows the primary system design parameters. These along with Chapter 8 of Fermilab-TM-2136, "The Proton Driver Design Study," are used as the basis for this design. The parameters are the same as in PD1 except for the average pressure, system length and aperture.

Table 5.4.1. Vacuum System Design Parameters

Average Pressure	$< 2 \times 10^{-7}$ Torr
Total System Length	474 m
Vacuum Aperture	4-in \times 6-in
Maximum Pump Spacing	N/A
Primary Pump Type	Ion Pump, 800 l/s.
Roughing Pump Type	Turbo Molecular (500 l/s), w/10 CFM Dry Backing Pump.
Sector Pump-down Time	12 hr to rough vacuum, 72 hr bake-out to high vacuum.
Vacuum Gauging	Pirani, Ion Gauge and Ion Pump Read-back.
Beam Tube Material	Straight Sections and Magnets without Eddy Current Heating (Stainless Steel), Magnets with Eddy Current Heating (Inconel)
Vacuum Interface Type	Flanged with bellows.
Special Considerations	Dipoles and Quadrupoles of vacuum canned design (core and coils will be in the vacuum space).
Bake-out System	Magnet vacuum chambers will need low temperature ($<150^{\circ}$ C) bake-out capability.

As with PD1, all components that make up the vacuum system will need to be fabricated using ultra-high vacuum (UHV) practices and a low temperature bake-out system will need to be built into the magnets. It is premature at this time to lay out vacuum sector lengths, but in general they will need to be short enough to facilitate operational bake-outs. This will probably limit sector lengths to three or four long dipoles.

Most of the differences between the PD2 and PD1 vacuum systems are due to the changes in magnet properties and lengths. The quadrupoles used in PD2 are shorter and smaller in cross section than those used in PD1. This results in an 80% reduction in gas load for the PD2 quadrupoles and the number of 800 l/s ion pumps can be reduced from two to one per quadrupole. The same is true for the short dipoles except that the ion pumps are reduced from four to two. The long dipoles are longer but smaller in cross section than those used in PD1. As a result only a 10% reduction in gas load is achieved. Therefore, four 800 l/s ion pumps will still be required per long dipole. This makes a total of 188 ion pumps needed for PD2 versus 384 for PD1.

The other significant change between PD2 and PD1 is the number of vacuum interfaces. PD1 had two interfaces per magnet for a total of 288. In PD2 the F and D quadrupoles come as a set, thereby reducing the number of vacuum interfaces to one per quadrupole. PD2 would have a total of 148 vacuum interfaces.

5.4.2 Performance

In addition to the geometry and length changes noted above, the average pressure required for PD2 has been increased to 2×10^{-7} Torr from 1×10^{-7} . This is significant in that we are now in a pressure range that tests have shown are achievable. After the writing of the PD1 study, out-gassing tests were done on the lamination and coil materials. The results indicate that the total pressure at the long dipole pumps would be between 1×10^{-7} and 2×10^{-7} Torr several days after a bake out for PD1. This pressure range was based on out-gassing data taken two days after the samples had been baked at 150°C for two to three days. Experience shows us that the out-gassing rates will continue to decrease for many weeks after a bake-out. It is therefore reasonable to assume that the ultimate pressure will be less than that indicated by the tests. Table 5.4.2 shows the anticipated partial pressures for the component gases in the long dipoles for PD2 and PD1, using the out-gassing data from the tests.

Table 5.4.2. Partial Pressure for Component Gases in Long Dipoles

Gas	% Gas	Partial Pressure in PD1 (Torr)	Partial Pressure in PD2 (Torr)
H ₂	58	6.8×10^{-8}	6.1×10^{-8}
CH ₄	5	5.4×10^{-9}	4.9×10^{-9}
H ₂ O	15	1.8×10^{-8}	1.6×10^{-8}
CO	18	2.1×10^{-8}	1.9×10^{-8}
CO ₂	4	4.2×10^{-9}	3.8×10^{-9}
Totals	100	1.2×10^{-7}	1.0×10^{-7}

5.5 Control System

M. Shea, J. Patrick

5.5.1 Fermilab Control System

The overall architecture of Fermilab control systems follows the standard design shown in Figure 5.5.1. Individual Front End Computers that control accelerator hardware are networked to each other, to console computers, and to various servers using a Local Area Network. The network connections contain 10 MHz, 100 MHz, and 1 GHz Ethernet segments along with switches and routers as needed, so that Control Room Consoles may access data for all the accelerators.

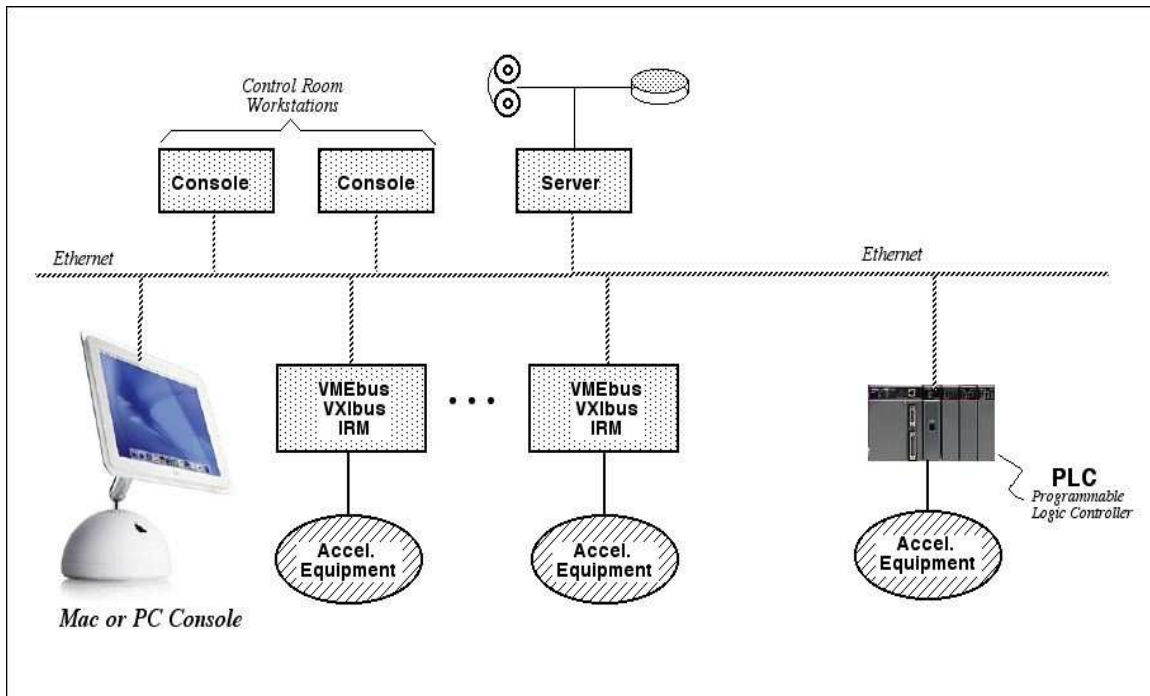


Figure 5.5.1. Control system architecture.

To the Fermilab Control System, the Proton Driver must appear as one more accelerator in the complex. It will be operated from the Main Control Room, and data from the Proton Driver will be presented on console displays along with data from other Fermilab accelerators.

The Control System architecture for PD2 will be essentially the same as that described in the PD1 design study, Fermilab-TM-2136. Because the machine operates at

15 Hz, the control system currently used for the Fermilab Linac, parts of the Booster, Tevatron and Main Injector will be used. This system is VMEbus-based, uses the Wind River vxWorks real time operating system and operates synchronously with the 15 Hz repetition rate of the accelerators. Both VMEbus crates and Internet Rack Monitors (IRMs) are used as Front End computers in the Fermilab ACNET control system. Operationally, the Proton Driver and its associated beam lines will appear as additional equipment to be controlled from ACNET consoles in the Main Control Room. The Front End computers connect to the accelerator hardware, collect raw data and make it available to ACNET.

5.5.2 PD2 Controls

The Control System for PD2 includes controls for the Linac, the synchrotron ring and the injection and extraction transport lines. Most of the controls for PD2 are similar to the controls needed for PD1. Because of that, the controls costs for many systems remain the same as those contained in the PD1 design study. The major change is due to the addition of a 200 MeV section of Linac although there are reductions in the requirements for the low energy end of the Linac and for the ring vacuum system.

5.5.2.1 PD2 Injection energy

The injection energy chosen for PD2 is 600 MeV, which requires the addition of 200 MeV of side-coupled cavity to be located in the injection tunnel. Five klystron stations are needed to provide the RF for this part of the Linac. Controls for this section of Linac will be similar to the high-energy end of the existing Linac. A VMEbus crate driving two HRMs will be used to control and monitor each of the five klystron stations. Beam diagnostics data will be collected using Quick Digitizer VMEbus modules. The beam diagnostics include wall current monitors, beam position detectors, wire scanners, and loss monitors. Except for the loss monitors, the beam diagnostic data will be acquired using 10 MHz snapshot digitizers.

5.5.2.2 Ion source and RFQ

The low energy part of the Linac for PD2 has been simplified compared with the system proposed for PD1. Instead of having two RFQ modules and the double alpha transport system, a single RFQ/ion source will be positioned very close to the input of the first Linac drift tube tank. This will reduce the RFQ system control costs, although an expanded offline test area would be needed to study the beam properties before mounting the assembly in place. Linac control costs have been reduced by about 30% to reflect this change.

5.5.2.3 Vacuum System

In the vacuum controls area, the PD2 controls costs will decrease. There are fewer ion pumps in the PD2 ring and so the vacuum controls will decrease by 20%.

5.5.4 R&D Program

During the R&D phase of the Proton Driver program, two VMEbus modules should be developed: an 8-channel 10-20 MHz Quick Digitizer module, and an 8-channel programmable waveform generator to be used to drive correction element power supplies.